MATERIALS SCIENCE

Multi-principal elemental intermetallic nanoparticles synthesized via a disorder-to-order transition

Mingjin Cui[1]†, Chunpeng Yang[1]†, Sooyeon Hwang[2]†, Menghao Yang[1]†, Sean Overa[3]†, Qi Dong[1], Yonggang Yao[1], Alexandra H. Brozena[1], David A. Cullen[4], Miaofang Chi[4], Thomas F. Blum[4], David Morris[5], Zou Finfrock[6,7], Xizheng Wang[1], Peng Zhang[5], Vitaliy G. Goncharov[8], Xiaofeng Guo[8], Jian Luo[9], Yifei Mo[1]*, Feng Jiao[3]*, Liangbing Hu[1]*

Nanoscale multi-principal element intermetallics (MPEIs) may provide a broad and tunable compositional space of active, high–surface area materials with potential applications such as catalysis and magnetics. However, MPEI nanoparticles are challenging to fabricate because of the tendency of the particles to grow/agglomerate or phase-separated during annealing. Here, we demonstrate a disorder-to-order phase transition approach that enables the synthesis of ultrasmall (4 to 5 nm) and stable MPEI nanoparticles (up to eight elements). We apply just 5 min of Joule heating to promote the phase transition of the nanoparticles into $L1_0$ intermetallic structure, which is then preserved by rapidly cooling. This disorder-to-order transition results in phase-stable nanoscale MPEIs with compositions (e.g., PtPdAuFeCoNiCuSn), which have not been previously attained by traditional synthetic methods. This synthesis strategy offers a new paradigm for developing previously unexplored MPEI nanoparticles by accessing a nanoscale-size regime and novel compositions with potentially broad applications.

INTRODUCTION

Intermetallic compounds represent an important and unique family of metals that feature long-range atomic ordering with well-defined sublattices of the constituent metal or semimetal elements (*1*). Traditionally, bulk intermetallic materials or intermetallic precipitates in other bulk matrices have been primarily used for their mechanical properties (*2*, *3*). However, nanoscale intermetallics, with their large active surface area and unique surface properties, could prove to be highly useful for various applications such as catalysis (*4*, *5*), magnetics (*6*), and superconductivity (*7*). To date, intermetallic nanoparticles have been limited to binary (*8*–*15*) or ternary (*16*, *17*) compositions because of issues of particle growth/agglomeration and phase separation in the multimetallic alloy. As a result, previously demonstrated intermetallic nanoparticles have featured a narrow compositional space that has prevented the potential of these materials from being fully realized.

Synthesizing multi-principal element intermetallic (MPEI; more than three elements) nanoparticles requires fine control of the reaction conditions, which has been difficult to achieve by traditional synthesis methods (*18*) (e.g., furnace annealing) because of the slow heating/cooling rates. Specifically, the long heating durations of annealing-based techniques cause particle growth and agglomeration, preventing the synthesis of nanoscale MPEIs. An added complication is the thermodynamic immiscibility of the constituent elements, which results in phase separation (fig. S1) (*14*, *19*). While phase separation can be circumvented by recently developed kinetic trapping techniques (*20*), the resulting multimetallic nanoparticles are disordered solid-solution alloys [i.e., high-entropy alloys (HEAs)] (*21*) rather than ordered MPEI nanoparticles. As MPEI nanoparticles are projected to offer unique properties in catalysis (*4*, *5*), there is a clear need for a new synthetic approach that can achieve nanoscale MPEI materials.

In this work, we demonstrate the synthesis of nanoscale MPEIs (4 to 5 nm) that contain up to eight different elements without particle growth or phase separation via a unique multi-elemental disorder-to-order (HEA to MPEI) phase transition strategy (Fig. 1A). Specifically, we first rapidly Joule-heated metal salt precursors on the carbon substrate [x-ray diffraction (XRD) and scanning electron microscopy characterization in fig. S2] at ~1100 K for 55 ms to produce disordered solid-solution HEA nanoparticles as the starting material (*22*). We then use the precise heating control made possible by this Joule-heating approach (in which the reaction temperature is controlled by an electric current) to reheat the HEA nanoparticles for just 5 min at ~1100 K to promote atomic rearrangement to a more thermodynamically stable MPEI configuration (i.e., a disorder-to-order transition), followed by rapid cooling to lock the final ordered structure in place. The resulting MPEI nanoparticles feature an intermetallic structure that has two sublattices (A_1B_1) (fig. S3a). Taking the octonary $(Pt_{0.8}Pd_{0.1}Au_{0.1})(Fe_{0.6}Co_{0.1}Ni_{0.1}Cu_{0.1}Sn_{0.1})$ $L1_0$ MPEI that we synthesized as an example, high-angle annular dark-field scanning transmission electron microscopy (HAADF-STEM; Fig. 1B) showed that the noble metal atoms Pt, Pd, and Au randomly distribute in sublattice A (bright layers), while the non-noble metal atoms Fe, Co, Ni, Cu, and Sn randomly distribute in sublattice B (dark layers), forming the intermetallic structure (fig. S3b).

This approach demonstrates a general strategy to synthesize MPEI nanoparticles, not only providing a step toward octonary intermetallics but also enabling the synthesis of MPEIs at the nanoscale with a previously unidentified compositional space in an

[1]Department of Materials Science and Engineering, University of Maryland, College Park, MD 20742, USA. [2]Center for Functional Nanomaterials, Brookhaven National Laboratory, Upton, NY 11973, USA. [3]Department of Chemical and Biomolecular Engineering, Center for Catalytic Science and Technology, University of Delaware, Newark, DE 19716, USA. [4]Center for Nanophase Materials Science, Oak Ridge National Laboratory, Oak Ridge, TN 37831, USA. [5]Department of Chemistry, Dalhousie University, Halifax, NS 15000, Canada. [6]Advanced Photon Source, Argonne National Laboratory, Lemont, IL 60439, USA. [7]Science Division, Canadian Light Source Inc., 44 Innovation Boulevard, Saskatoon, SK S7N 2V3, Canada. [8]Department of Chemistry and Alexandra Navrotsky Institute for Experimental Thermodynamics, Washington State University, Pullman, WA 99164, USA. [9]Department of NanoEngineering, Program of Materials Science and Engineering, University of California San Diego, La Jolla, CA 92093, USA.
*Corresponding author. Email: binghu@umd.edu (L.H.); jiao@udel.edu (F.J.); yfmo@umd.edu (Y.M.)
†These authors contributed equally to this work.

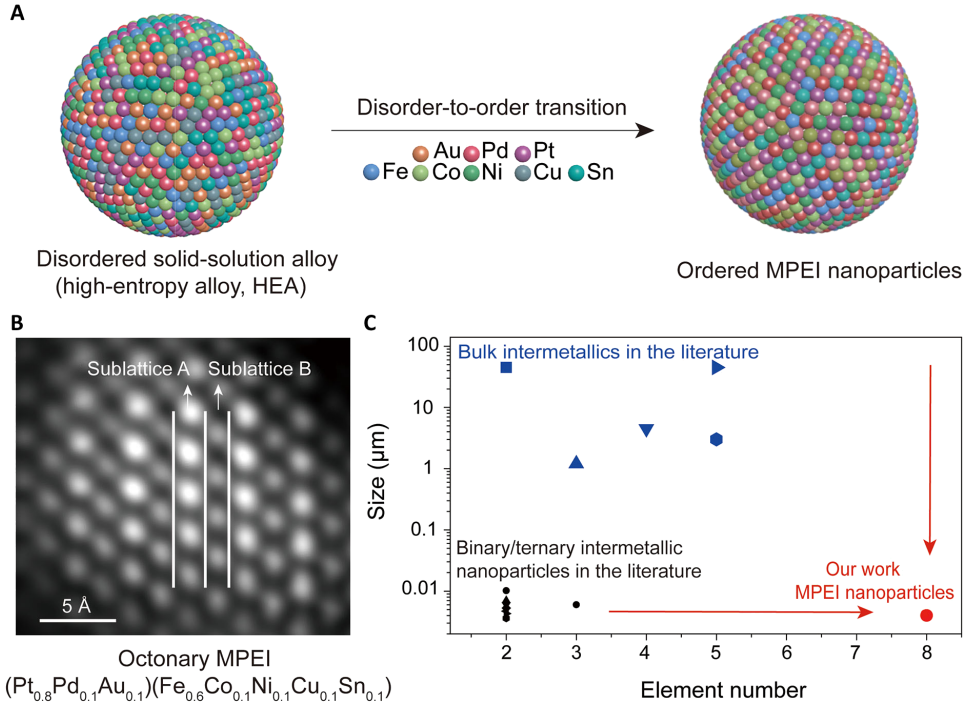

Fig. 1. MPEI nanoparticle synthetic process, product, and comparison with the literature. (**A**) Schematic of the disorder-to-order phase transition from a multielemental disordered solid-solution (HEA) nanoparticle to an MPEI nanoparticle with an ordered $L1_0$ structure, enabled by Joule heating. (**B**) HAADF-STEM image of an octonary $(Pt_{0.8}Pd_{0.1}Au_{0.1})(Fe_{0.6}Co_{0.1}Ni_{0.1}Cu_{0.1}Sn_{0.1})$ MPEI nanoparticle synthesized by our approach, in which the noble metal atoms of Pt, Pd, and Au randomly distribute in sublattice A and the non-noble metal atoms of Fe, Co, Ni, Cu, and Sn randomly distribute in sublattice B, together forming the $L1_0$ intermetallic structure. (**C**) Compared with prior literature reports (see fig. S4 and tables S1 and S2) (*4*–*6*, *12*, *42*–*49*), this work significantly extends the elemental space of intermetallics at the nanoscale.

unexplored size regime (Fig. 1C, fig. S4, and tables S1 and S2). We anticipate that these findings can be extended to produce a combinatorial library of intermetallic nanomaterials that may feature novel properties and applications, potentially inducing a new frontier of intermetallic research and applications.

RESULTS

To synthesize the MPEI nanoparticles, we preloaded a carbon substrate with desired metal salt precursor combinations/ratios and Joule-heated (fig. S5) the materials with precise control of the temperature and heating/cooling rates by tuning the power applied to the substrate (fig. S6). The temperature profile and structural evolution of nanoparticles over time are illustrated in Fig. 2A. We first synthesize solid-solution (HEA) nanoparticles (*22*) by heating the metal precursors for tens of milliseconds at ~1100 K. This is a critical step for mixing the different elements without phase separation. A disorder-to-order phase transition is then achieved by rapidly reheating the materials to ~1100 K for an additional ~5 min—a limited amount of time that is sufficient to complete the desired transition from the disordered HEA structure to the ordered, single-phase MPEI configuration while simultaneously avoiding nanoparticle growth/agglomeration. Last, the single-phase MPEI structure and small particle size (~5 nm) is preserved by rapidly cooling the materials (~10^4 K/s).

To demonstrate the versatility of this synthesis, we fabricated binary, quinary, and octonary intermetallic nanoparticles and characterized them by atomic-resolution STEM and energy-dispersive x-ray spectroscopy (EDX). The PtFe binary and $Pt(Fe_{0.7}Co_{0.1}Ni_{0.1}Cu_{0.1})$ quinary intermetallic nanoparticles demonstrate small particle sizes and narrow size distributions of 5.4 ± 0.8 and 4.4 ± 0.5 nm, respectively (fig. S7). An HAADF-STEM image of a binary PtFe nanoparticle shows alternating layers of Fe (darker atoms) and Pt columns (brighter atoms) (Fig. 2B), which is typical of an $L1_0$ intermetallic structure. We then confirmed the ordered $L1_0$ structure of the binary PtFe sample from the interplanar spacings of 3.71, 2.73, and 2.20 Å in the STEM images, which correspond to the (001), (110), and (111) facets of the ordered $L1_0$ structure along the [110] direction, respectively (*23*).

Similarly, the quinary $Pt(Fe_{0.7}Co_{0.1}Ni_{0.1}Cu_{0.1})$ nanoparticles showed alternating darker columns of Fe, Co, Ni, and Cu atoms and brighter columns of Pt atoms (Fig. 2C). Atomic-resolution EDX mapping indicates that the well-defined Pt atoms are in one sublattice, while the Fe, Co, Ni, and Cu atoms are uniformly distributed in the other sublattice, both with the $L1_0$ structure. According to the fitted extended x-ray absorption fine structure (EXAFS) (fig. S8 and table S3), the coordination number of Fe-Pt (6) is much larger than that of Fe-Cu (1.2), Cu-Fe (1.0), Co-Ni (2.0), and Ni-Co (2). These results are in accordance with the $L1_0$ structure in which the Fe—Cu, Cu—Fe, Co—Ni, and Ni—Co bonds in the quinary intermetallic are localized and limited to two-dimensional layer bonding in the ordered structure, while the Fe-Pt bonding occurs in a three-dimensional structure in the intermetallic. We also synthesized quinary MPEI nanoparticles with different elemental ratios (fig. S9) and different intermetallic structure [e.g., the $L1_2$ phase of $(Pt_{0.8}Au_{0.1}Pd_{0.1})_3(Fe_{0.9}Co_{0.1})$; fig. S10], showcasing the potential of this rapid/limited heating method to broaden the scope of possible intermetallic materials. Last, we

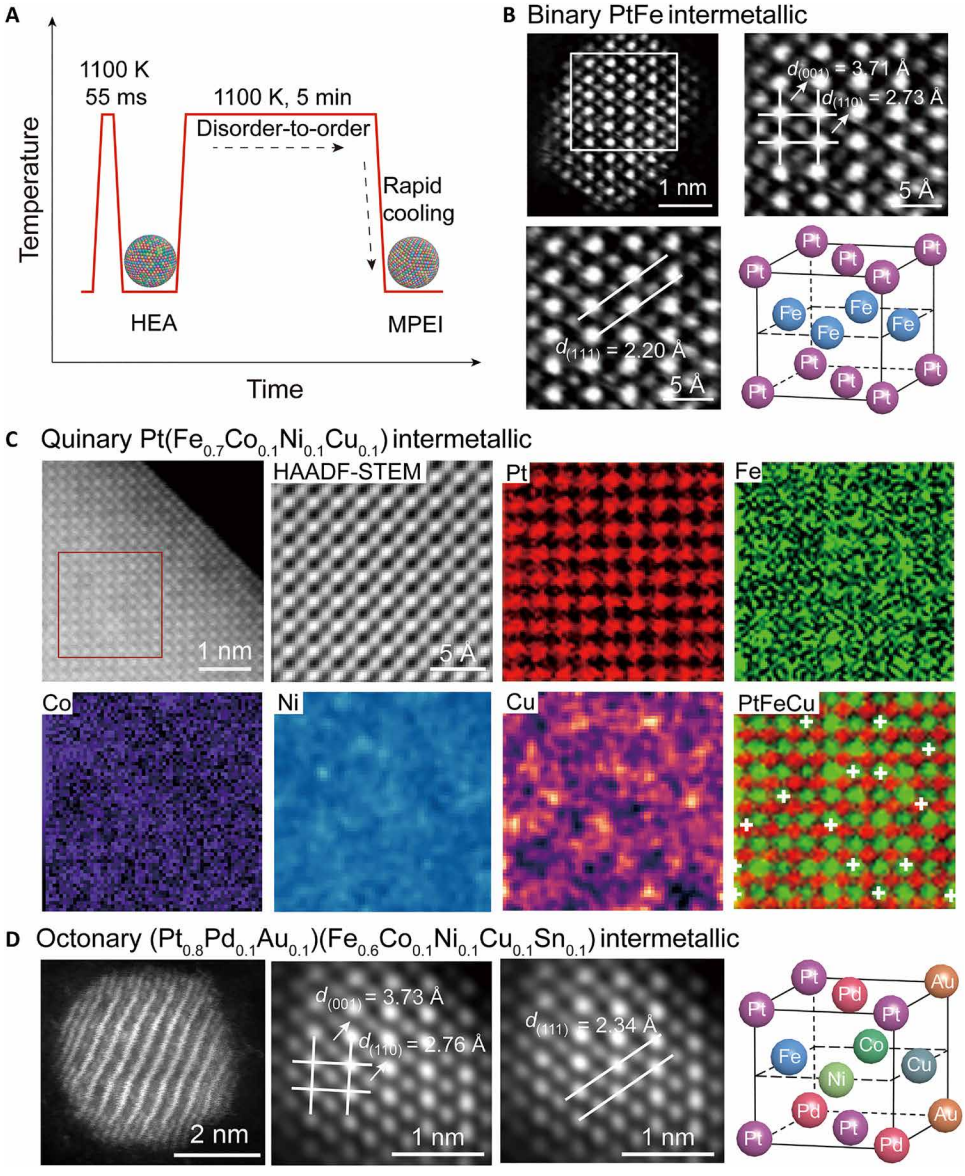

Fig. 2. The synthesis and characterization of the binary, quinary, and octonary intermetallic nanoparticles. (**A**) The formation of the MPEI nanoparticles in the Joule-heating process, with respect to the temperature evolution as a function of the heating time. (**B**) HAADF-STEM image of the ordered binary PtFe nanoparticle along with its lattice structure. (**C**) A HAADF-STEM image of a quinary Pt($Fe_{0.7}Co_{0.1}Ni_{0.1}Cu_{0.1}$) MPEI nanoparticle and the corresponding atomic-resolution EDX mapping (the EDX analysis region is shown in the red square). The position of the Cu atoms was identified by finding the local maxima from the Cu EDX map after Gaussian filtering, which was overlaid on the Pt-Fe EDX map (shown in red and green, respectively). (**D**) HAADF-STEM image of an octonary ($Pt_{0.8}Pd_{0.1}Au_{0.1}$)($Fe_{0.6}Co_{0.1}Ni_{0.1}Cu_{0.1}Sn_{0.1}$) MPEI nanoparticle along with its lattice structure.

synthesized octonary ($Pt_{0.8}Pd_{0.1}Au_{0.1}$)($Fe_{0.6}Co_{0.1}Ni_{0.1}Cu_{0.1}Sn_{0.1}$) nanoparticles (fig. S11), which featured (001), (110), and (111) planes with spacings of 3.73, 2.76, and 2.34 Å, respectively, in the STEM image (Fig. 2D), also forming an $L1_0$ intermetallic structure. Thus, our process based on a disorder-to-order transition enables the synthesis of nanoscale MPEIs with multiple elements (up to eight) as well as different elemental ratios and various intermetallic structures.

In contrast, it is very difficult to synthesize nanoscale MPEIs without phase separation via traditional annealing methods (*24*). As a control, we prepared octonary $Pt_{0.8}Pd_{0.1}Au_{0.1}Fe_{0.6}Co_{0.1}Ni_{0.1}Cu_{0.1}Sn_{0.1}$ nanoparticles by traditional annealing (*24*) (~1100 K, 3 hours) and found that they formed phase-separated heterostructures without the desired atomic ordering according to STEM imaging (fig. S12) and XRD (fig. S13). Phase separation occurs because the slow heating/cooling rates of traditional annealing result in large particle size and distribution (~76.2 ± 4.2 nm; fig. S14) of the octonary $Pt_{0.8}Pd_{0.1}Au_{0.1}Fe_{0.6}Co_{0.1}Ni_{0.1}Cu_{0.1}Sn_{0.1}$ nanoparticles, different from the MPEI nanoparticles (~5 nm) synthesized by our method. Thus, only in our approach do we avoid phase separation, which is made possible by starting with HEA nanoparticles that already have the constituent elements well mixed. The limited heating duration of the technique also enables the disorder-to-order transition while

preventing particle growth to successfully produce MPEI nanoparticles. In addition, the octonary composition that we determined by inductively coupled plasma mass spectroscopy demonstrates a slight difference from the molar ratio of the precursors (table S4), likely due to the different vapor pressures of metals. To achieve precise compositional control, we can compensate for this slightly vaporization loss by adjusting the initial precursor loading according to the vapor pressure of different metals (table S4).

To further investigate the disorder-to-order phase transition that enables MPEI formation, we synthesized an array of quinary Pt($Fe_{0.7}Co_{0.1}Ni_{0.1}Cu_{0.1}$) samples that were heated at ~1100 K for different amounts of time and performed XRD to characterize their degree of ordering (Fig. 3A). According to our calculated virtual XRD pattern, the diffraction peaks of (001) at 24.2° and (110) at 33.4° are the superlattice peaks of the ideal $L1_0$ intermetallic structure of Pt($Fe_{0.7}Co_{0.1}Ni_{0.1}Cu_{0.1}$). On the basis of the intensities of these peaks, we quantified the ordering degree of the different quinary samples using the long-range ordering (LRO) parameter, which is defined by (*25*)

$$\mathrm{LRO} = \frac{I_{110}/I_{111}}{I_{110}^{*}/I_{111}^{*}} \times 100\%$$

where I_{110} and I_{111} are the peak intensities of the superlattice (110) and nonsuperlattice (111) diffraction peaks, respectively, and I^* is the corresponding peak intensity of the perfectly ordered $L1_0$ structure (LRO = 100%). We observed no superlattice diffraction peaks for the sample made with only 0.05 s of Joule heating, suggesting that the short heating time is incapable of inducing the disorder-to-order phase transition for $Pt_1Fe_{0.7}Co_{0.1}Ni_{0.1}Cu_{0.1}$. As we increased the heating time from 0.5 s to 5 min, the characteristic diffraction peaks of $L1_0$, (001) and (110), gradually intensified. As a result, the LRO increased from 10 (0.5 s) to 60% (1 min) and lastly, ~100% (5 min) (fig. S15), demonstrating the disorder-to-order phase transition process that completes after 5 min of heating. The Rietveld refinement of the XRD results of the quinary Pt($Fe_{0.7}Co_{0.1}Ni_{0.1}Cu_{0.1}$) MPEI (fig. S16 and table S5) also reveals the formation of the fully ordered $L1_0$ intermetallic structure of the sample heated for 5 min, in which the Co, Ni, Cu, and Fe elements occupy one sublattice and Pt occupies the other sublattice.

The effect of the heating temperature and time on the LRO of the quinary Pt($Fe_{0.7}Co_{0.1}Ni_{0.1}Cu_{0.1}$) is shown in Fig. 3B, which demonstrates that we can achieve ~100% LRO only by Joule heating at ~1100 K for ~5 min. This disorder-to-order transition process (0.5 s to 5 min) is also consistent with our STEM imaging of the quinary Pt($Fe_{0.7}Co_{0.1}Ni_{0.1}Cu_{0.1}$) MPEI nanoparticles synthesized at ~1100 K for different heating durations (fig. S17), which shows that the disordered HEA nanoparticle structure converts to an MPEI structure over the course of ~5-min heating.

We find that this disorder-to-order phase transition toward single-phase MPEIs consisting of immiscible elements can only be achieved at the nanoscale. For quinary Pt($Fe_{0.7}Co_{0.1}Ni_{0.1}Cu_{0.1}$) nanoparticles, the fully ordered $L1_0$ structure (LRO = 100%) can be obtained in particles of 4 to 5 nm. However, for larger particles, we find that the LRO decreases with the particle size (Fig. 3C), irrespective of the particle synthesis method (slow cooling or longer heating time; figs. S18 and S19). When the particle size increases to ~60 nm or larger, the particle shows disordered or other phase-separated heterostructures, as confirmed by STEM and EDX (Fig. 3D).

We also conducted Monte Carlo (MC) simulations of different-sized nanoparticles and tracked their LRO change as a function of the MC steps (corresponding to the reaction time) at 1100 K to further understand the transition at the nanoscale (Fig. 3E). The LROs of particles of 3.1 and 4.6 nm in size increase with the MC steps, and then both reach ~100% within 3×10^7 steps, meaning that both particles have completed the disorder-to-order phase transition at this point of the simulation progress. However, for a particle that is 7.7 nm in size, only a partial disorder-to-order transition (LRO = 40%) can be achieved after 3×10^7 simulation steps. The largest particle that we simulated at 10.8 nm shows an even lower LRO of 5% after the same number of MC simulation steps. These findings (Fig. 3E) are consistent with our experimental observations using XRD [Fig. 3A (5 min) and figs. S18 and S19] and STEM (Fig. 3D), in which the complete disorder-to-order phase transition is primarily achieved and stabilized in ultrasmall nanoparticles (<5 nm).

We attribute the size effect on the disorder-to-order transition to the difference in surface energy. MPEIs have a lower surface energy than HEAs, as MPEIs forms stronger atom-atom interactions (*26*). Because of the large relative surface area of small nanoparticles, we hypothesize that the difference in the surface energy between MPEI and HEA small nanoparticles (~5 nm) play a key role in driving the disorder-to-order transition. It is also possible that the larger particles (e.g., 10 to 20 nm) need to overcome a higher energy barrier to complete the disorder-to-order transition (*27*). For the particles substantially larger than 5 nm (e.g., 150 nm), such a large energy barrier could hinder the formation of fully ordered MPEIs.

The disorder-to-order transition is thermodynamically favored to form phase-stable MPEI nanoparticles. We verified the lower enthalpy of the MPEI nanoparticles with a size of 4 to 5 nm by conducting high-temperature oxide melt drop solution calorimetry (*28*) on the quinary and octonary MPEIs and their corresponding disordered HEA starting materials. According to the calorimetry measurements (tables S6 and S7), the enthalpy change from the quinary HEA to MPEI was −0.20 eV per Pt($Fe_{0.7}Co_{0.1}Ni_{0.1}Cu_{0.1}$) formula, and, for the octonary HEA to MPEI, the enthalpy change was −0.32 eV per ($Pt_{0.8}Pd_{0.1}Au_{0.1}$)($Fe_{0.6}Co_{0.1}Ni_{0.1}Cu_{0.1}Sn_{0.1}$) formula, indicating that the ordered MPEIs are thermodynamically favored.

We also simulated this disorder-to-order phase transition through MC modeling (*29*) of the atomic arrangement of the quinary Pt($Fe_{0.7}Co_{0.1}Ni_{0.1}Cu_{0.1}$) nanoparticle at 1100 K (Fig. 4A and movie S1), which shows the atoms of the disordered HEA starting material diffusing to form the ordered MPEI, similar to the transition process in other intermetallics (*8*, *26*). During the transition, the formation enthalpy (ΔH_f) of the quinary MPEI decreases substantially (Fig. 4B), driven by the strong interaction via the spin-orbit coupling and the hybridization between non-noble metal 3*d* and noble 5*d* states. The decreased enthalpy leads to a lower Gibbs free energy of the MPEI (G_o) than that of the HEA (G_d) sample (based on the same quinary composition Pt$Fe_{0.7}Co_{0.1}Ni_{0.1}Cu_{0.1}$) at a wide temperature range (~273 to 1500 K), according to MC modeling (Fig. 4C). At temperatures below 1500 K (and above the decomposition temperature of the metal salts; table S8), the low enthalpy of the MPEIs dominates the Gibbs free energy and thus $G_o < G_d$. Therefore, at the synthesis temperature (~1100 K), the disorder-to-order transition is thermodynamically favored ($\Delta G_{d \to o} = G_o - G_d < 0$), and, at room temperature, the ordered MPEI is the thermodynamically stable phase (Fig. 4C).

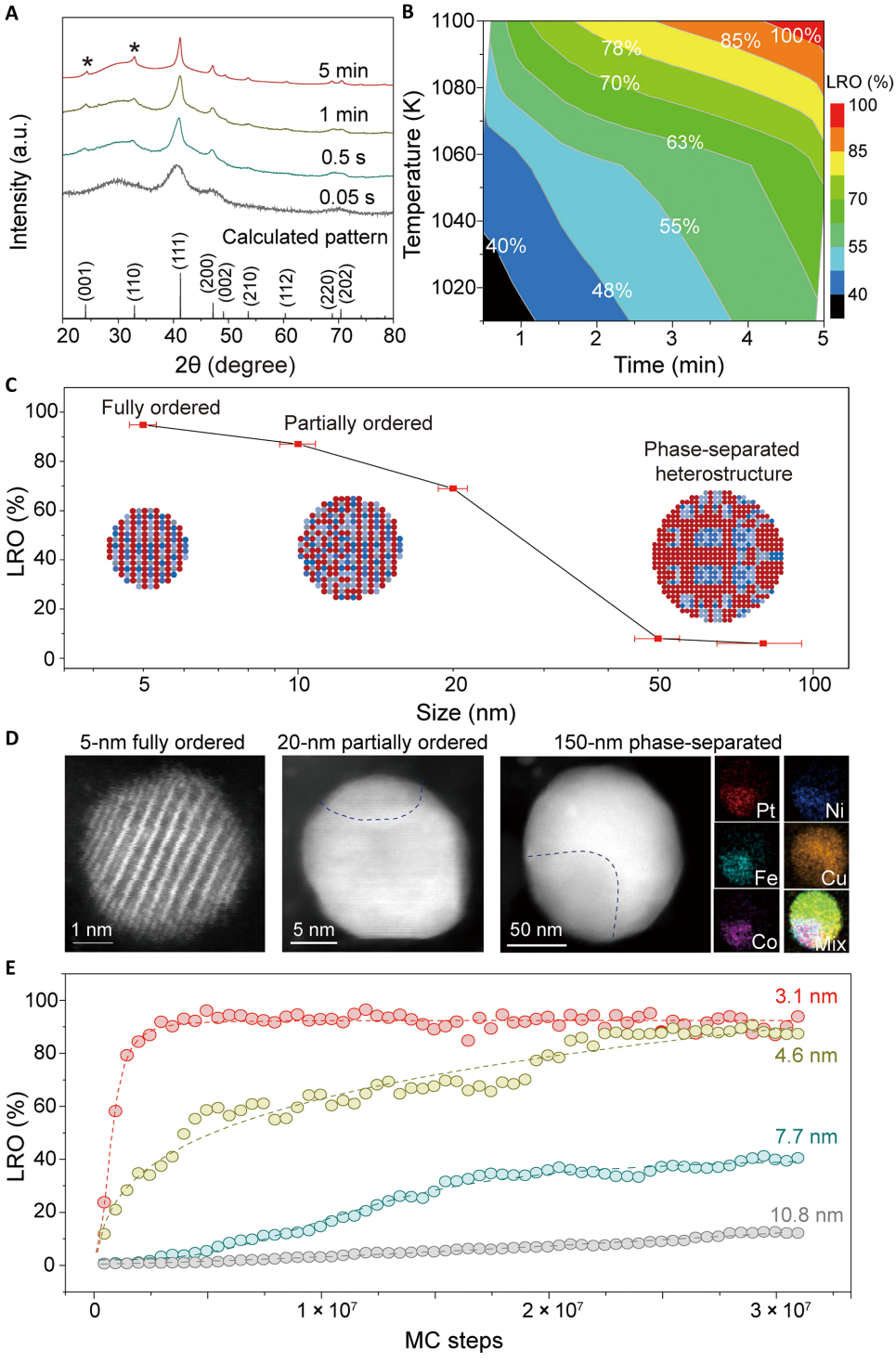

Fig. 3. The disorder-to-order phase transition process of MPEIs at the nanoscale. (**A**) Experimental XRD patterns of the quinary Pt($Fe_{0.7}Co_{0.1}Ni_{0.1}Cu_{0.1}$) synthesized at different heating times at a temperature of ~1100 K and the virtual XRD pattern of the fully ordered quinary Pt($Fe_{0.7}Co_{0.1}Ni_{0.1}Cu_{0.1}$) MPEI computed by the virtual XRD analysis method (*40*). The asterisk (*) represents the superlattice peaks of the intermetallic. a.u., arbitrary units. (**B**) The time and temperature dependence of the LRO of the quinary Pt($Fe_{0.7}Co_{0.1}Ni_{0.1}Cu_{0.1}$). (**C**) The LRO as a function of the quinary MPEI particle size. The insets schematically show the microstructural evolution as a function of the particle size. (**D**) HAADF-STEM images of nanoparticles of increasing size (~5, 20, and 150 nm), in which the smallest nanoparticle features an ordered structure, while the larger particles become increasingly disordered, corresponding to the schematics in (C). EDX mapping of the 150-nm particle shows its phase-separated structure. (**E**) The simulated LROs of different-sized nanoparticles (3.1, 4.6, 7.7, and 10.8 nm) as a function of the MC simulation steps.

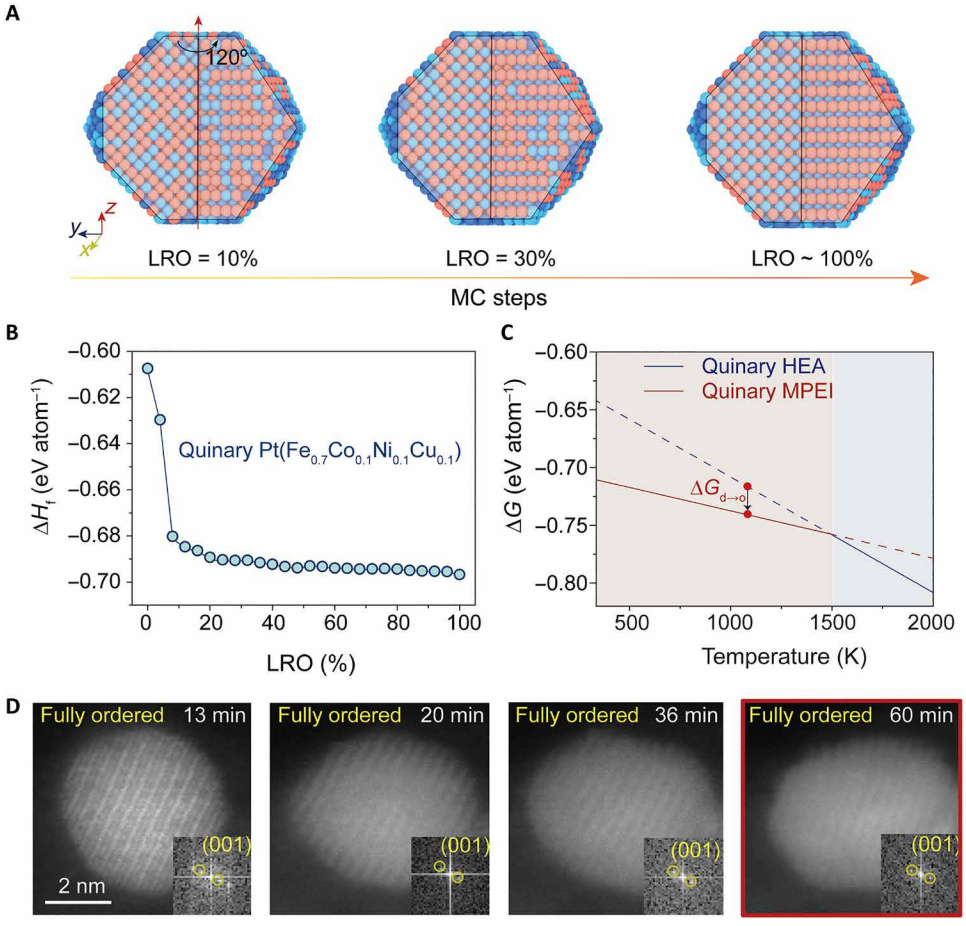

Fig. 4. The thermodynamic stability of MPEI nanoparticles. (**A**) Simulated three-dimensional lattice images of the quinary $Pt(Fe_{0.7}Co_{0.1}Ni_{0.1}Cu_{0.1})$ disorder-to-order phase transition process at 1100 K, from LRO = 10% to ~100% with increased MC steps (which is correlated to the transition time). (**B**) The formation enthalpy (ΔH_f) of the quinary $Pt(Fe_{0.7}Co_{0.1}Ni_{0.1}Cu_{0.1})$ nanoparticle as a function of the LRO. (**C**) The calculated Gibbs free energies of the quinary MPEI (LRO = 100%) and the disordered quinary HEA (LRO = 0) (both with a composition of $PtFe_{0.7}Co_{0.1}Ni_{0.1}Cu_{0.1}$) as a function of temperature. (**D**) Time-resolved HAADF-STEM images demonstrating the phase stability of an isolated ordered quinary $Pt(Fe_{0.7}Co_{0.1}Ni_{0.1}Cu_{0.1})$ nanoparticle as it is heated at ~1100 K over the course of 60 min.

Upon completing the disorder-to-order transition, we found that the ultrasmall MPEI nanoparticles displayed excellent phase stability, as evidenced by in situ heating a quinary $Pt(Fe_{0.7}Co_{0.1}Ni_{0.1}Cu_{0.1})$ MPEI nanoparticle and simultaneously monitoring its phase evolution by STEM (Fig. 4D). The quinary MPEI nanoparticle synthesized by Joule heating displayed a fully ordered structure even after 13 min of additional heating at ~1100 K, as indicated by the (001) diffraction spot in the fast Fourier transform (FT) image. We then held the nanoparticle at ~1100 K for another 47 min and still did not observe a phase change, indicating the thermal stability of the MPEI nanoparticle. In contrast, the binary PtFe nanoparticles (~5 nm) at ~1100 K showed an ordered intermetallic structure (14 min) but gradually transformed to a disordered alloy (60 min), indicating the superior thermal stability of MPEIs compared to binary intermetallics (fig. S20).

We can achieve MPEI nanoparticles on different carbon substrates (e.g., carbonized wood, carbon nanofiber, carbon black, and reduced graphene oxide) (fig. S21). To demonstrate the application of the MPEI nanoparticles, we manufacture octonary $(Pt_{0.8}Pd_{0.1}Au_{0.1})(Fe_{0.6}Co_{0.1}Ni_{0.1}Cu_{0.1}Sn_{0.1})$ MPEI nanoparticles on Ketjenblack carbon support (fig. S22), which demonstrates the superiority of the MPEI nanoparticles as an electrocatalyst for ethanol oxidation reaction (EOR). EOR is the key reaction in direct alcohol fuel cells, which are considered one of the most promising electric power sources (fig. S23). However, EOR requires efficient catalysts with high surface area, tunable composition, and good stability, which could be fulfilled by nanoscale MPEI materials. MPEI nanoparticles demonstrate improved EOR activity that is 8 and 12 times higher than the binary PtFe intermetallic and commercial Pt/C catalyst, respectively (fig. S24) (*30*–*32*). The octonary MPEI nanoparticles demonstrate excellent durability during long-term catalytic operation (fig. S25). This could be attributed to the material's multi-elemental composition, ordered intermetallic structure, and nanosize.

DISCUSSION

In summary, we report the first synthesis of MPEI nanoparticles with up to eight constituent elements through a unique disorder-to-order phase transition. This transition is achieved by starting with disordered, solid-solution HEA nanoparticles that are Joule-heated for a short period of time (~5 min) followed by rapid cooling (~10^4 K/s).

The HEA starting materials synthesized through a rapid thermal shock (tens of milliseconds heating) enables the mixing of the diverse elements, regardless of their thermodynamic miscibility. The subsequent ~5 min of heating is then critical to achieve the disorder-to-order transition that converts the HEA nanoparticles into MPEI nanoparticles, which is driven by thermodynamic stability. In addition, the limited heating time and the ensuing rapid temperature quenching prevent the MPEI nanoparticles from excessive growth and agglomeration. This unique approach not only produces stable MPEIs at the nanoscale but also can enable previously unidentified MPEI compositions (e.g., PtPdAuFeCoNiCuSn) that have never been achieved by traditional methods because of the inherent immiscibility of the elements. This work opens the material space of possible intermetallic nanomaterials, with potential in catalysis, magnetics, superconductivity, and more.

MATERIALS AND METHODS

Precursor loading

The nanoparticles were synthesized by Joule heating on a carbonized wood substrate. Basswood was purchased from Walnut Hollow Company and cut into slices of 1.5 cm by 0.5 cm by 0.5 cm in size. The wood slices were then treated at 533 K in air for 6 hours with a heating rate of 5 K min^{-1} and then 1273 K in argon flow for another 6 hours to carbonize. The resulting wood substrate was further activated at 1023 K in the flow of CO_2 for 6 hours to introduce surface defects.

We dissolved the precursors H_2PtCl_6, $PdCl_2$, $HAuCl_4$, $FeCl_3$, $CoCl_2$, $NiCl_2$, $CuCl_2$, and $SnCl_2$ (purchased from Sigma-Aldrich with a purity of ≥99.9%) in ethanol (0.05 M). The precursor solutions (binary PtFe, quinary $PtFe_{0.7}Co_{0.1}Ni_{0.1}Cu_{0.1}$/$Pt_1Fe_{0.25}Co_{0.25}Ni_{0.25}Cu_{0.25}$, and octonary $Pt_{0.8}Pd_{0.1}Au_{0.1}Fe_{0.6}Co_{0.1}Ni_{0.1}Cu_{0.1}Sn_{0.1}$) were mixed at stoichiometric ratios and dropped onto the carbon substrate with a micropipette at a loading of ~800 μl cm^{-2}. The two ends of the carbon substrate were suspended on glass slides and connected to two copper electrodes with silver paste. The precursor-loaded carbon substrates were then dried in a 353-K oven for 6 hours and used directly for the Joule-heating method (*33*).

For comparison, carbonized wood prepared in the same manner as described above was used as the substrate to synthesize binary PtFe and octonary $Pt_{0.8}Pd_{0.1}Au_{0.1}Fe_{0.6}Co_{0.1}Ni_{0.1}Cu_{0.1}Sn_{0.1}$ nanoparticles by a traditional thermal reduction method (*24*) that involved heating the precursor-loaded carbon substrates at ~1100 K for 3 hours in Ar/H_2 flow (95:5 ratio) in a tube furnace.

Joule-heating method

Direct electrical Joule heating of the precursor-loaded carbon substrates was triggered in an argon-filled glove box by a Keithley 2425 Source Meter Supply with adjustable current and duration. Electrical pulses with different duration times (0.05 and 0.5 s and 1 and 5 min) were applied to the carbon substrate to generate the desired temperature and heating time to synthesize the MPEIs.

Spectrum collection and fitting

During the Joule-heating process, the emitted light from the sample was captured by a time-resolved pyrometer (Vision Research Phantom Miro M110 high-speed camera) (*34*). The captured emission spectrum was fitted to the blackbody radiation to obtain the fitted parameters

$$B_\lambda = (\lambda, T) = \delta \frac{2hc^2}{\lambda^5} \frac{1}{e^{\frac{hc}{\lambda k_B T}} - 1} \quad (1)$$

where k_B is the Boltzmann constant, h is the Planck constant, c is the speed of light, λ is the wavelength, and δ is a constant introduced for the fitting.

High-temperature oxide melt drop solution calorimetry

High-temperature oxide melt drop solution calorimetry measurements were conducted using a Tian-Calvet twin microcalorimeter, Setaram AlexSys-1000 (*28*). $Pt(Fe_{0.7}Co_{0.1}Ni_{0.1}Cu_{0.1})$ nanoparticles supported on carbon black samples were pressed into ~1 mg of pellets using a hand die. The pellets were then added into a molten sodium molybdate ($3NaO{\cdot}4MoO_3$) solvent within a platinum crucible at 700°C. O_2 gas was continuously flushed through the calorimetric chamber at 95 ml min^{-1} to maintain a constant gas environment over the solvent. The complete dissolution of the quinary samples can be reached in the molten $3NaO{\cdot}4MoO_3$ solvent, allowing effective determination of the enthalpy of the drop solution (ΔH_{ds}), which is directly measured by the calorimeter. ΔH_{ds} consists of the heat content of the sample at 700°C, the enthalpy of the oxidation reactions, and the enthalpy of the dissolution of the sample in the solvent. After removing the enthalpy of oxidation of the carbon black substrate from ΔH_{ds}, we obtained the corrected enthalpies of the drop solution ($\Delta H_{ds}'$) that are only associated with the quinary HEA and MPEI samples. These corrections were done on the basis of the corresponding thermochemical reactions described in table S6. Instrument calibration procedures and in-depth descriptions of the calorimetric methodologies can be found in previous reports (*35*).

Structural characterization

Part of the HAADF-STEM images were acquired with a Hitachi HD2700C–dedicated scanning transmission electron microscope with a probe Cs corrector. STEM-EDX elemental mapping were obtained with an FEI Talos F200X. Both microscopes were operated at an accelerating voltage of 200 kV. A DENSsolutions Wildfire holder was used for the in situ STEM heating experiment. We pretreated the precursors (~1100 K for 0.2 s) to remove the harmful chlorine gas produced during the metal precursor decomposition process, which could damage the microscope combined atomic-resolution STEM and EDX results were acquired on a JEOL NeoARM scanning transmission electron microscope operated at 80 kV and equipped with dual silicon drift detectors. The STEM image was simultaneously acquired with EDX mapping (after wiener filtering). XRD was performed using a D8 ADVANCE (Bruker AXS, WI, USA) with a scan rate of 0.5° min^{-1}. EXAFS analysis was performed using the CLS@APS [Sector 20–bending magnet (BM)] beamline at the Advanced Photon Source (operating at 7.0 GeV) at Argonne National Laboratory. Co, Cu, Fe, and Ni K-edge and Pt L_3-edge data were collected from solid samples placed on Kapton tape and measured in fluorescence mode simultaneously with a foil reference for each element. The EXAFS data were transformed and normalized into *k*- and *R*-space using the Athena program following conventional procedures. A *k* weighting of 2 was used to obtain all FT-EXAFS spectra. The *k*-range used for each element was as follows: 2.2 to 10.7 $Å^{-1}$ for Co, 3.3 to 13.2 $Å^{-1}$ for Cu, 3.5 to 10.6 $Å^{-1}$ for Fe, 2.3 to 10.5 $Å^{-1}$ for Ni, and 3.0 to 12.9 $Å^{-1}$ for Pt. The *R*-range used for each element was as follows: 1.2 to 3.5 Å for Co, 1.0 to 3.3 Å for Cu, 1.0 to 3.2 Å for Fe, 1.0 to 3.3 Å for Ni, and 1.0 to 3.3 Å for Pt. Self-consistent multiple-scattering calculations

were performed using the FEFF6 program to obtain the scattering amplitudes and phase shift functions used to fit various scattering paths with the Artemis program. In the fitting of all samples, the E_0 values were correlated together to minimize the number of independent values, allowing reliable fitting results to be obtained. In addition, the Debye-Waller factor values for the metal-metal paths in Co, Cu, and Ni were correlated together. For Fe, all the Debye-Waller factor values were correlated together.

Computational analysis

MC modeling

Quinary Pt($Fe_{0.7}Co_{0.1}Ni_{0.1}Cu_{0.1}$) nanoparticles with different particle sizes were investigated by canonical ensemble MC simulations based on the Metropolis algorithm and combined binary Pt-*M* (*M* = Fe, Co, Ni, and Cu) potentials (*36*–*38*). The lattice models of Pt($Fe_{0.7}Co_{0.1}Ni_{0.1}Cu_{0.1}$) were established with truncated octahedral shapes that had different diameters of 3.1, 4.6, 7.1, and 10.8 nm, corresponding to 1289, 4033, 29881, and 46929 atoms, respectively. In each MC step, two atoms were randomly selected and interchanged with a probability according to the Metropolis algorithm (*39*).

MC modeling was performed at 1100 K. Each configuration generated at every 50,000 MC steps was analyzed by virtual XRD. The LRO were calculated on the basis of the intensity ratio of the calculated superlattice peak (110) and nonsuperlattice peak (111). The entropy of each configuration was calculated on the basis of Eq. 2

$$S^{\mathrm{IM}} = -R\left[\sum_{x=1}^{x} a_x \sum_{i=1}^{N} f_i^x \ln(f_i^x)\right] / \sum_{x=1}^{x} a_x \quad (2)$$

where S^{IM} is the the configurational entropy of the MPEI, f_i^x is the fraction of element species *i* randomly distributed on the *x* sublattice in the quinary Pt($Fe_{0.7}Co_{0.1}Ni_{0.1}Cu_{0.1}$), *N* is the total number of element species *i*, and a_x is the number of sites on the *x* sublattice. For the (Pt, Pd, Au)(Fe, Co, Ni, Cu, Sn) structure, there are two sublattices, *x* and *y*; the number of sublattice sites are $a_x = 1$ and $a_y = 1$.

The enthalpy of the quinary Pt($Fe_{0.7}Co_{0.1}Ni_{0.1}Cu_{0.1}$) was calculated by Eq. 3

$$E_0 - \sum_{i=1}^{N} f_i E_i H = E_0 - \sum_{M=1}^{N_0} f_M E_M \quad (3)$$

in which E_0 is the formation energy of the quinary Pt($Fe_{0.7}Co_{0.1}Ni_{0.1}Cu_{0.1}$), and f_M and E_M are the fraction and energy of the transition metal element species *M* (Pt, Fe, Co, Ni, and Cu). N_0 is the total number of transition metal element species *M*. $E_{\text{Pt-}M}$ is the formation energy of bimetallic Pt-*M*. A total of 1000 configurations were collected to obtain the averaged values of the formation energy, entropy, and LRO.

Configurational entropy disordered alloys

The configurational entropy of disordered alloys (HEA) can be calculated according to Eq. 4 (*14*)

$$S^{\mathrm{Dis}} = -R\left[\sum_{i=1}^{N} f_i^x \ln(f_i^x)\right] \quad (4)$$

where S^{Dis} is the configurational entropy of the disordered alloy, *R* is the gas constant, f_i^x is the molar fraction of the element species *i*, and *N* is the total number of element species.

Virtual XRD analysis

XRD line profiles were created by virtually rotating the Ewald sphere around the origin of reciprocal space to all possible orientations, mimicking powder diffraction conditions (*40*). Typically, the XRD patterns were performed on the basis of the virtual diffraction analysis, using a wavelength of 1.542 Å (Cu Kα as the virtual radiation source) at a temperature of ~1100 K.

Electrochemical measurements for EOR

Electrode preparation

Catalyst inks were prepared by dispersing ~10 mg of catalyst [octonary ($Pt_{0.8}Pd_{0.1}Au_{0.1}$)($Fe_{0.6}Co_{0.1}Ni_{0.1}Cu_{0.1}Sn_{0.1}$) MPEI nanoparticles with a loading of 29 weight % (wt %) on carbon black and binary PtFe intermetallic nanoparticles with a loading of 28.7 wt % on carbon black] in 2 ml of a 1:1 mixture of isopropyl alcohol (ACS Reagent) and deionized water. Nafion ionomer (5 wt %) was added to act as a binder. The mixtures were sonicated for 1 hour to ensure complete dispersion of the catalyst in solution. The inks were then drop-casted onto carbon paper (Sigracet 39 BB, Fuel Cell Store) until the desired loading was reached. Electrodes were dried overnight at 70°C in air to ensure that all the solvent was evaporated. Commercial Pt/C catalyst was purchased from Sigma-Aldrich.

Cyclic voltammetry experiments

Tests were performed in an H-type cell using a FAA-3-50 membrane as a divider. A solution of 1 M KOH (pellets, 99.98% metal basis, Thermo Fisher Scientific) and 1 M ethanol (200 proof, Decon Labs, Thermo Fisher Scientific) was used as the electrolyte for the experiments. To remove any metal ions from the solution, a chelating agent (Chelex 100 sodium form, Sigma-Aldrich) was added to the solution and stirred overnight. Electrochemical experiments were performed using a Pt wire counter electrode and a Hg/HgO reference electrode (Koslow Scientific). Electrochemical measurements were done using an Autolab PGSTAT204 (Metrohm). Cyclic voltammetry (CV) was performed by sweeping from 0.2 to 1.2 V [versus reversible hydrogen electrode (RHE)] for 250 scans at a scan rate of 50 mV s^{-1}. After the initial 250 scans, the electrolyte was replaced with fresh solution, and an additional 50 scans were run. Electrolyte was degassed with argon (99.999%, Keen Gas), and the headspace was kept under argon atmosphere for the duration of the experiments.

Electrochemical surface area measurements were done using a Cu underpotential deposition procedure (*32*). Electrodes were first cleaned in a solution of 0.5 M H_2SO_4 by scanning from 0 to 1 V versus RHE at 250 mV s^{-1} for multiple scans, using a Ag/AgCl reference electrode (Pine Research) and a Pt wire counter electrode. Baseline CVs were then collected by scanning from 0 to 1 V (versus RHE) at 25 mV s^{-1}. Cu underpotential deposition was performed in a solution of 0.5 M H_2SO_4 and 5 mM $CuSO_4$. Electrodes were held at a constant potential of 0.3 V (versus RHE) for 300 s to ensure complete coverage of the active sites on the catalysts and then were swept from that potential to 1 V (versus RHE) at 25 mV s^{-1}. The charges associated with copper stripping were obtained by using the charge associated with any oxide growth subtracting the charge obtained use the same conditions in 0.5 M H_2SO_4. The electrochemical surface area was determined using the value of 410 μC cm^{-2} (*41*).

SUPPLEMENTARY MATERIALS

Supplementary material for this article is available at https://science.org/doi/10.1126/sciadv.abm4322

REFERENCES AND NOTES

1. Y. Yang, C.-C. Chen, M. C. Scott, C. Ophus, R. Xu, A. Pryor Jr., L. Wu, F. Sun, W. Theis, J. Zhou, M. Eisenbach, P. R. C. Kent, R. F. Sabirianov, H. Zeng, P. Ercius, J. Miao,

Deciphering chemical order/disorder and material properties at the single-atom level. *Nature* **542**, 75–79 (2017).
2. T. M. Smith, B. D. Esser, N. Antolin, A. Carlsson, R. E. A. Williams, A. Wessman, T. Hanlon, H. L. Fraser, W. Windl, D. W. Mccomb, M. J. Mills, Phase transformation strengthening of high-temperature superalloys. *Nat. Commun.* **7**, 13434 (2016).
3. A. Heckl, S. Neumeier, M. Göken, R. F. Singer, The effect of Re and Ru on γ/γ′ microstructure, γ-solid solution strengthening and creep strength in nickel-base superalloys. *Mater. Sci. Eng. A* **528**, 3435–3444 (2011).
4. D. L. Wang, H. L. Xin, R. Hovden, H. S. Wang, Y. C. Yu, D. A. Muller, F. J. Disalvo, H. D. Abruña, Structurally ordered intermetallic platinum-cobalt core-shell nanoparticles with enhanced activity and stability as oxygen reduction electrocatalysts. *Nat. Mater.* **12**, 81–87 (2013).
5. D. Kim, J. Resasco, Y. Yu, A. M. Asiri, P. D. Yang, Synergistic geometric and electronic effects for electrochemical reduction of carbon dioxide using gold-copper bimetallic nanoparticles. *Nat. Commun.* **5**, 4948 (2014).
6. S. H. Sun, C. B. Murray, D. Weller, L. Folks, A. Moser, Monodisperse FePt nanoparticles and ferromagnetic FePt nanocrystal superlattices. *Science* **287**, 1989–1992 (2000).
7. S. M. Clarke, J. P. S. Walsh, M. Amsler, C. D. Malliakas, T. Yu, S. Goedecker, Y. B. Wang, C. Wolverton, D. E. Freedman, Discovery of a superconducting Cu-Bi intermetallic compound by high-pressure synthesis. *Angew. Chem. Int. Ed.* **55**, 13446–13449 (2016).
8. J. Liang, F. Ma, S. Hwang, X. Wang, J. Sokolowski, Q. Li, G. Wu, D. Su, Atomic arrangement engineering of metallic nanocrystals for energy-conversion electrocatalysis. *Joule* **3**, 956–991 (2019).
9. X. Wang, S. Hwang, Y.-T. Pan, K. Chen, Y. He, S. Karakalos, H. Zhang, J. S. Spendelow, D. Su, G. Wu, Ordered Pt_3Co intermetallic nanoparticles derived from metal-organic frameworks for oxygen reduction. *Nano Lett.* **18**, 4163–4171 (2018).
10. Y. Qiu, L. Xin, Y. Li, I. T. Mccrum, F. Guo, T. Ma, Y. Ren, Q. Liu, L. Zhou, S. Gu, M. J. Janik, W. Li, BCC-phased PdCu alloy as a highly active electrocatalyst for hydrogen oxidation in alkaline electrolytes. *J. Am. Chem. Soc.* **140**, 16580–16588 (2018).
11. C. Wang, D. P. Chen, X. Sang, R. R. Unocic, S. E. Skrabalak, Size-dependent disorder–order transformation in the synthesis of monodisperse intermetallic PdCu nanocatalysts. *ACS Nano* **10**, 6345–6353 (2016).
12. S. P. Luo, W. Chen, Y. Cheng, X. Song, Q. L. Wu, L. X. Li, X. T. Wu, T. H. Wu, M. R. Li, Q. Yang, K. R. Deng, Z. W. Quan, Trimetallic synergy in intermetallic PtSnBi nanoplates boosts formic acid oxidation. *Adv. Mater.* **31**, 1903683 (2019).
13. Y. Xiong, Y. Yang, H. Joress, E. Padgett, U. Gupta, V. Yarlagadda, D. N. Agyeman-Budu, X. Huang, T. E. Moylan, R. Zeng, A. Kongkanand, F. A. Escobedo, J. D. Brock, F. J. Disalvo, D. A. Muller, H. D. Abruna, Revealing the atomic ordering of binary intermetallics using in situ heating techniques at multilength scales. *Proc. Natl. Acad. Sci. U.S.A.* **116**, 1974–1983 (2019).
14. D. Miracle, O. Senkov, A critical review of high entropy alloys and related concepts. *Acta Mater.* **122**, 448–511 (2017).
15. L. Wang, Z. H. Zeng, W. P. Gao, T. Maxson, D. Raciti, M. Giroux, X. Q. Pan, C. Wang, J. Greeley, Tunable intrinsic strain in two-dimensional transition metal electrocatalysts. *Science* **363**, 870–874 (2019).
16. J. Zhu, Y. Yang, L. X. Chen, W. P. Xiao, H. F. Liu, H. D. Abruna, D. L. Wang, Copper-induced formation of structurally ordered Pt-Fe-Cu ternary intermetallic electrocatalysts with tunable phase structure and improved stability. *Chem. Mater.* **30**, 5987–5995 (2018).
17. T. Wang, J. Liang, Z. Zhao, S. Li, G. Lu, Z. Xia, C. Wang, J. Luo, J. Han, C. Ma, Y. Huang, Q. Li, Sub-6 nm fully ordered $L1_0$-Pt-Ni-Co nanoparticles enhance oxygen reduction via Co doping induced ferromagnetism enhancement and optimized surface strain. *Adv. Energy Mater.* **9**, 1803771 (2019).
18. P. C. Chen, X. L. Liu, J. L. Hedrick, Z. Xie, S. Z. Wang, Q. Y. Lin, M. C. Hersam, V. P. Dravid, C. A. Mirkin, Polyelemental nanoparticle libraries. *Science* **352**, 1565–1569 (2016).
19. J. Park, M. K. Kabiraz, H. Kwon, S. Park, H. Baik, S. I. Choi, K. Lee, Radially phase segregated PtCu@PtCuNi dendrite@frame nanocatalyst for the oxygen reduction reaction. *ACS Nano* **11**, 10844–10851 (2017).
20. S. M. Dou, J. Xu, X. Y. Cui, W. D. Liu, Z. C. Zhang, Y. D. Deng, W. B. Hu, Y. N. Chen, High-temperature shock enabled nanomanufacturing for energy-related applications. *Adv. Energy Mater.* **10**, 2001331 (2020).
21. J. C. Feng, D. Chen, P. V. Pikhitsa, Y.-H. Jung, J. Yang, M. Choi, Unconventional alloys confined in nanoparticles: Building blocks for new matter. *Matter* **3**, 1646–1663 (2020).
22. Y. G. Yao, Z. N. Huang, P. F. Xie, S. D. Lacey, R. J. Jacob, H. Xie, F. J. Chen, A. M. Nie, T. C. Pu, M. Rehwoldt, D. W. Yu, M. R. Zachariah, C. Wang, R. Shahbazian-Yassar, J. Li, L. B. Hu, Carbothermal shock synthesis of high-entropy-alloy nanoparticles. *Science* **359**, 1489–1494 (2018).
23. X. Du, Y. He, X. Wang, J. Wang, Fine-grained and fully ordered intermetallic PtFe catalysts with largely enhanced catalytic activity and durability. *Energ. Environ. Sci.* **9**, 2623–2632 (2016).
24. Q. Wang, Z. L. Zhao, Z. Zhang, T. L. Feng, R. Y. Zhong, H. Xu, S. T. Pantelides, M. Gu, Sub-3 nm intermetallic ordered Pt_3In clusters for oxygen reduction reaction. *Adv. Sci.* **7**, 1901279 (2020).
25. V. Karanasos, I. Panagiotopoulos, D. Niarchos, H. Okumura, G. C. Hadjipanayis, CoPt/Ag nanocomposites with (001) texture. *Appl. Phys. Lett.* **79**, 1255–1257 (2001).
26. Y. C. Yan, J. S. S. Du, K. D. Gilroy, D. R. Yang, Y. N. Xia, H. Zhang, Intermetallic nanocrystals: Syntheses and catalytic applications. *Adv. Mater.* **29**, 1605997 (2017).
27. F. Huang, J. F. Banfield, Size-dependent phase transformation kinetics in nanocrystalline ZnS. *J. Am. Chem. Soc.* **127**, 4523–4529 (2005).
28. A. Navrotsky, Progress and new directions in calorimetry: A 2014 perspective. *J. Am. Ceram. Soc.* **97**, 3349–3359 (2014).
29. B. Lee, B. D. Wirth, J.-H. Shim, J. Kwon, S. C. Kwon, J.-H. Hong, Modified embedded-atom method interatomic potential for the Fe-Cu alloy system and cascade simulations on pure Fe and Fe-Cu alloys. *Phys. Rev. B* **71**, 184205 (2005).
30. W. Y. Zhang, Y. Yang, B. L. Huang, F. Lv, K. Wang, N. Li, M. C. Luo, Y. G. Chao, Y. J. Li, Y. J. Sun, Z. K. Xu, Y. N. Qin, W. X. Yang, J. H. Zhou, Y. P. Du, D. Su, S. J. Guo, Ultrathin PtNiM (M = Rh, Os, and Ir) nanowires as effcient fuel oxidation electrocatalytic materials. *Adv. Mater.* **31**, 1805833 (2019).
31. J. Bai, X. Xiao, Y. Y. Xue, J. X. Jiang, J. H. Zeng, X. F. Li, Y. Chen, Bimetallic platinum-rhodium alloy nanodendrites as highly active electrocatalyst for the ethanol oxidation reaction. *ACS Appl. Mater. Interfaces* **10**, 19755–19763 (2018).
32. D. S. Wu, K. Kusada, T. Yamamoto, T. Toriyama, S. Matsumura, S. Kawaguchi, Y. Kubota, H. Kitagawa, Platinum-group-metal high-entropy-alloy nanoparticles. *J. Am. Chem. Soc.* **142**, 13833–13838 (2020).
33. Y. N. Chen, G. C. Egan, J. Y. Wan, S. Z. Zhu, R. J. Jacob, W. B. Zhou, J. Q. Dai, Y. B. Wang, V. A. Danner, Y. G. Yao, K. Fu, Y. B. Wang, W. Z. Bao, T. Li, M. R. Zachariah, L. B. Hu, Ultra-fast self-assembly and stabilization of reactive nanoparticles in reduced graphene oxide films. *Nat. Commun.* **7**, 12332 (2016).
34. X. Wang, Z. Huang, Y. G. Yao, H. Y. Qiao, G. Zhong, Y. Pei, C. L. Zheng, D. Kline, Q. Q. Xia, Z. W. Lin, J. Q. Dai, M. R. Zachariah, B. Yang, R. S. Yassar, L. B. Hu, Continuous 2000 K droplet-to-particle synthesis. *Mater. Today* **35**, 106–114 (2020).
35. A. A. Voskanyan, V. G. Goncharov, N. Novendra, X. Guo, A. Navrotsky, Thermodynamics drives the stability of the MOF-74 family in water. *ACS Omega* **5**, 13158–13163 (2020).
36. G. U. Jeong, C. S. Park, H. S. Do, S. M. Park, B. Lee, Second nearest-neighbor modified embedded-atom method interatomic potentials for the Pd-M (M = Al, Co, Cu, Fe, Mo, Ni, Ti) binary systems. *Calphad* **62**, 172–186 (2018).
37. J. Kim, Y. Koo, B. Lee, Modified embedded-atom method interatomic potential for the Fe-Pt alloy system. *J. Mater. Res.* **21**, 199–208 (2006).
38. M. Müller, P. Erhart, K. Albe, Thermodynamics of $L1_0$ ordering in FePt nanoparticles studied by Monte Carlo simulations based on an analytic bond-order potential. *Phys. Rev. B* **76**, 155412 (2007).
39. W. K. Hastings, Monte carlo sampling methods using Markov chains and their applications. *Biometrika* **57**, 97–109 (1970).
40. S. P. Coleman, D. E. Spearot, L. Capolungo, Virtual diffraction analysis of Ni [0 1 0] symmetric tilt grain boundaries. *Model. Simul. Mater. Sci. Eng.* **21**, 055020 (2013).
41. C. L. Green, A. Kucernak, Determination of the platinum and ruthenium surface areas in platinum-ruthenium alloy electrocatalysts by underpotential deposition of copper. I. unsupported catalysts. *J. Phys. Chem. B* **106**, 1036–1047 (2002).
42. D. Alloyeau, C. Ricolleau, C. Mottet, T. Oikawa, C. Langlois, Y. L. Bouar, N. Braidy, A. Loiseau, Size and shape effects on the order–disorder phase transition in CoPt nanoparticles. *Nat. Mater.* **8**, 940–946 (2009).
43. D. Y. Desario, F. J. Disalvo, Ordered intermetallic Pt-Sn nanoparticles: Exploring ordering behavior across the bulk phase diagram. *Chem. Mater.* **26**, 2750–2757 (2014).
44. J. R. Li, Z. Xi, Y. T. Pan, J. S. Spendelow, P. N. Duchesne, D. Su, Q. Li, C. Yu, Z. Y. Yin, B. Shen, Y. S. Kim, P. Zhang, S. H. Sun, Fe stabilization by intermetallic $L1_0$-FePt and Pt catalysis enhancement in $L1_0$-FePt/Pt nanoparticles for efficient oxygen reduction reaction in fuel cells. *J. Am. Chem. Soc.* **140**, 2926–2932 (2018).
45. J. H. Hwang, T. T. T. Trang, O. Lee, G. Park, A. Zargaran, N. J. Kim, Improvement of strength-ductility balance of B2-strengthened lightweight steel. *Acta Mater.* **191**, 1–12 (2020).
46. B. Niu, Z. H. Wang, Q. Wang, Q. F. Pan, C. Dong, R. Q. Zhang, H. Q. Liu, P. K. Liaw, W. Xu, Dual-phase synergetic precipitation in Nb/Ta/Zr co-modified Fe–Cr–Al–Mo alloy. *Intermetallics* **124**, 106848 (2020).
47. G. Park, C. H. Nam, A. Zargaran, N. J. Kim, Effect of B2 morphology on the mechanical properties of B2-strengthened lightweight steels. *Scr. Mater.* **165**, 68–72 (2019).
48. T. Yang, Y. L. Zhao, Y. Tong, Z. B. Jiao, J. Wei, J. X. Cai, X. D. Han, D. Chen, A. Hu, J. J. Kai, K. Lu, Y. Liu, C. T. Liu, Multicomponent intermetallic nanoparticles and superb mechanical behaviors of complex alloys. *Science* **362**, 933–937 (2018).
49. Z. Y. Liu, H. Z. Wang, M. Haché, E. Irissou, Y. Zou, Formation of refined grains below 10 nm in size and nanoscale interlocking in the particle–particle interfacial regions of cold sprayed pure aluminum. *Scr. Mater.* **187**, 280–284 (2020).

Acknowledgments: We acknowledge the support of the Maryland NanoCenter, its Surface Analysis Center, and AIMLab. We thank D. Kline and M. R. Zachariah at the University of

Maryland, College Park for the assistance in MATLAB coding for the high-temperature Joule-heating measurement. **Funding:** Y.M. acknowledges the funding support from the National Science Foundation (NSF) under award number 2004837 and the computational facilities from the University of Maryland supercomputing resources and the Maryland Advanced Research Computing Center (MARCC). J.L. acknowledges the support of the University of California Irvine Materials Research Science and Engineering Centers, Center for Complex and Active Materials, under NSF grant no. DMR-2011967. Atomic-resolution STEM-EDX was conducted at the Center for Nanophase Materials Sciences, which is a U.S. Department of Energy (DOE) Office of Science User Facility. The electron microscopy work used resources at the Center for Functional Nanomaterials, which is a DOE Office of Science Facility at Brookhaven National Laboratory under contract no. DE-SC0012704. This research used resources of the Advanced Photon Source, an Office of Science User Facility operated for the DOE Office of Science by Argonne National Laboratory, and was supported by the DOE under contract no. DE-AC02- 06CH11357 and the Canadian Light Source and its funding partners. **Author contributions:** L.H., M.Cui, and C.Y. designed the experiments. M.Cui and C.Y. carried out the material synthesis via high-temperature Joule heating. S.H. performed STEM characterizations. M.Y. performed MC and molecular dynamics simulations under the supervision of Y.M. M.Chi, D.A.C., and T.F.B. performed atomic-resolution EDX measurements. X.W. measured the temperature of the carbon substrate during the Joule heating. D.M., Z.F., and P.Z. contributed to the x-ray absorption measurements and analysis. V.G.G. and X.G. performed the high-temperature oxide melt drop solution calorimetry measurements. M.Cui, C.Y., and L.H. collectively wrote the paper. All authors commented on the final manuscript. **Competing interests:** The authors declare that they have no competing interests. **Data and materials availability:** All data needed to evaluate the conclusions in the paper are present in the paper and/or the Supplementary Materials.

Submitted 17 September 2021
Accepted 7 December 2021
Published 28 January 2022
10.1126/sciadv.abm4322